Optical Engineering

SPIEDigitalLibrary.org/oe

Noise properties and signal-dependent interpixel crosstalk of the detectors of the Near-Infrared Spectrograph of the James Webb Space Telescope

Giovanna Giardino
Marco Sirianni
Stephan M. Birkmann
Bernard J. Rauscher
Don Lindler
Torsten Böker
Pierre Ferruit
Guido De Marchi
Martin Stuhlinger
Peter Jensen
Paolo Strada

SPIE

Optical Engineering 52(3), 034001 (March 2013)

Noise properties and signal-dependent interpixel crosstalk of the detectors of the Near-Infrared Spectrograph of the James Webb Space Telescope

Giovanna Giardino
Marco Sirianni
Stephan M. Birkmann
European Space Agency
European Space Research and Technology Centre
Keplerlaan 1
2200AG Noordwijk, The Netherlands
E-mail: Giovanna.Giardino@esa.int

Bernard J. Rauscher
Don Lindler
NASA Goddard Space Flight Center
Mail Code 130
Greenbelt, Maryland 20771

Torsten Böker
Pierre Ferruit
Guido De Marchi
European Space Agency
European Space Research and Technology Centre
Keplerlaan 1
2200AG Noordwijk, The Netherlands

Martin Stuhlinger
European Space Agency
European Space Astronomy Centre
P.O. Box 78
Villanueva de la Cañnada, Spain

Peter Jensen
Paolo Strada
European Space Agency
European Space Research and Technology Centre
Keplerlaan 1
2200AG Noordwijk, The Netherlands

Abstract. The Near-Infrared Spectrograph (NIRSpec) is one of the four science instruments of the James Webb Space Telescope. Its focal plane consists of two HAWAII-2RG sensors operating in the wavelength range of 0.6 to 5.0 μm and, as part of characterizing NIRSpec, the noise properties of these detectors under dark and illuminated conditions were studied. Under dark conditions, and as already known, $1/f$ noise in the detector system causes somewhat higher noise levels than can be accounted for by a simple model that includes white read noise and shot noise on integrated charge. More surprisingly, for high levels of accumulated charge, significantly lower total noise than expected was observed. This effect is shown to be due to pixel-to-pixel correlations introduced by signal-dependent interpixel crosstalk, with an interpixel coupling factor, α, that ranges from ~0.01 for zero signal to ~0.03 close to saturation. *© 2013 Society of Photo-Optical Instrumentation Engineers (SPIE)* [DOI: 10.1117/1.OE.52.3.034001]

Subject terms: James Webb Space Telescope; near-infrared spectrograph; near-infrared detectors; noise; crosstalk.

Paper 121688P received Nov. 19, 2012; revised manuscript received Feb. 14, 2013; accepted for publication Feb. 15, 2013; published online Mar. 6, 2013.

1 Introduction

The Near-Infrared Spectrograph (NIRSpec) is a near-infrared multiobject spectrograph and one of the four science instruments of the James Webb Space Telescope (JWST).[1] NIRSpec is being developed by the European Space Agency (ESA) with European Aeronautic Defence and Space Company Astrium Germany GmbH as the prime contractor and it will be the first slit-based astronomical multiobject spectrograph (MOS) to fly in space. A selectable 3″ × 3″ integral field unit (IFU) and five fixed slits are also available for detailed spectroscopic studies of single objects.

All three NIRSpec modes (MOS, IFU, and fixed slits) share the need for large-format, high quantum efficiency, and ultra low-noise detectors covering the $\lambda = 0.6$ to 5 μm spectral range. This need is fulfilled by two 2048 × 2048 pixel (18 μm pixel pitch), 5.3 μm cutoff, Teledyne HAWAII-2RG (H2RG) sensor chip assemblies (SCAs), provided by NASA Goddard. H2RG is short for HgCdTe astronomy wide area infrared imager with reference pixels and guide mode (see Beletic et al.[2] for more details on these detectors). These IR sensors are hybrid complementary metal oxide semiconductor (CMOS) arrays, with HgCdTe used for light detection and a silicon integrated circuit for signal readout. Similar detectors will be used by the other NIR instruments on board JWST (NIRCam and NIRISS) as well as by future ESA mission, EUCLID.[3] Previous generations of this type of detectors are in use in Hubble Space Telescope (HST) Wild Field Camera 3 (HAWAII-1R)[4] and in instruments of ground facilities such as the near-infrared integral field spectrograph at Gemini North at Mauna Kea (HAWAII-2)[5] or X-shooter at the European Southern Observatory at Paranal (H2RG).[6]

This paper describes the overall noise properties of the two detector arrays (called, respectively, SCA491 and

---

0091-3286/2013/$25.00 © 2013 SPIE

SCA492) in NIRSpec focal plane FPA 104 and provides insights into some nonideal behaviors that have been observed in these early flight model detectors. The paper is organized as follows: after a brief introduction of NIRSpec detectors in Sec. 2, their overall noise properties are presented in Sec. 3. From these measurements, it is apparent that, at high levels of accumulated charge, one observes significantly lower total noise than expected. The origin of this anomaly is identified and characterized in Sec. 4 and these findings are then discussed in Sec. 5.

2 NIRSpec Detectors

JWST's H2RG detectors[2,7] achieve very low dark currents ($<0.01\ e^- s^{-1}\ \mathrm{pixel}^{-1}$) and high quantum efficiency (80% to 90%) over a wide bandpass.[8] The two H2RG SCAs for NIRSpec focal plane, together with the two application-specific integrated circuits that control them, were delivered to ESA, integrated and characterized, by the NIRSpec Detector Subsystem team of Goddard Space Flight Center in the fall of 2010, together with the detector system (DS) test data set.

For most science observations, NIRSpec detectors acquire up-the-ramp sampled data at a constant cadence of about one frame every 10.74 s. A frame is the unit of data that results from sequentially clocking through and reading out a rectangular area of pixels. Most often, this will be all of the pixels in the SCA, although smaller subarrays are also possible when faster cadences are needed, e.g., to observe bright targets. The data are said to be sampled up-the-ramp because the signal is nondestructively read out at regular intervals throughout the duration of the exposure; therefore, the signal, in each pixel, can be seen to "ramp" up. In a given exposure, the up-the-ramp samples can be individual frames, or the average of a number of frames (see Rauscher et al.[9] for more details on the instrument readout scheme).

Following HST-Near Infrared Camera and Multi-Object Spectrometer, this readout pattern is dubbed MULTIACCUM, frequently abbreviated as MULTI-$n \times m$, where n is the number of equally spaced groups sampling up the ramp and m is the number of averaged frames per group. This means that, for each pixel, each of the n values read while accumulating signals is the result of the average of m samples. In other words, a full-frame NIRSpec raw H2RG flexible image transport system file has a dimensionality of $2048 \times 2048 \times n$. Each group, in turn, is the result of averaging m frames of 2048×2048 pixels. From this data set, the count rate for each pixel is derived by linear least square fitting of the n up-the-ramp samples acquired during the exposure for that pixel.

To compute an exposure total noise when using multiple nondestructive reads, one must take into account the correlation between the samples. In the idealized situation where the only noise components are white readout noise and shot noise on integrated charge, Rauscher et al.[9,10] have shown that the general expression for the total noise variance of an electronically shuttered instrument using MULTIACCUM readout is

$$\sigma^2_{\mathrm{total}} = \frac{12(n-1)}{mn(n+1)}\sigma^2_{\mathrm{read}} + \frac{6(n^2+1)}{5n(n+1)}(n-1)t_g f - \frac{2(m^2-1)(n-1)}{mn(n+1)}(m-1)t_f f. \tag{1}$$

In this equation, σ_{total} is the total noise in units of e^- rms, σ_{read} is the read noise per frame in units of e^- rms, and f is the flux in units of $e^-\ s^{-1}\ \mathrm{pixel}^{-1}$, where f includes photonic current and dark current (for the special case of dark integrations, $f = i_{\mathrm{dark}}$); t_f is the frame time, i.e., the time interval between reading the first pixel in one frame and reading the same pixel in the next frame, while the group time t_g is simply the frame time multiplied by the number of frames per group.

To characterize the total noise of our detectors and compare it to the theoretical expectation using Eq. (1), we selected dark and flat-field exposures from the DS test data set.

3 Total Noise of NIRSpec Detectors

The subset of DS test data that we processed and analyzed consists of 100 dark exposures, 50 flat-field exposures at a "low" flux level of $f \sim 1.2\ e^-\ s^{-1}\ \mathrm{pixel}^{-1}$, and 25 flat-field exposures at a high flux level of $f \sim 150\ e^-\ s^{-1}\ \mathrm{pixel}^{-1}$. The darks and high-flux exposures were taken with a MULTI-88×1 readout pattern (thus $n = 88$ and $m = 1$), whereas for the low-flux exposures only 10 groups up-the-ramp were acquired (thus $n = 10$ and $m = 1$). In our case $t_g = t_f = 10.74$ s.

To compute the expected total noise using Eq. (1), a measure of the detector read noise is necessary. As discussed in Rauscher et al.,[9] under ultralow photon flux and ultralow dark current conditions, $\sigma_{\mathrm{read}} \approx \sigma_{\mathrm{CDS}}\sqrt{2}$, where CDS stands for correlated double sampling. This means that we can estimate the read noise variance from the variance of the difference of two adjacent groups in dark exposures. From two (arbitrarily chosen) dark exposures, a data cube containing 88 independent differences of two adjacent groups was constructed; the standard deviation, with iterative 3σ-rejection, over these 88 images was then computed for each pixel, providing a map of σ_{CDS}, from which a map of σ_{read} is readily derived. The median values of σ_{read} for our detectors are 12.6 and 11.9 e^-, respectively, for SCA491 and SCA492.

To compute the total noise, each exposure MULTIACCUM cube was first processed to derive the count rate image. This involves the following steps: bias subtraction, reference pixel subtraction, linearity correction, and up-the ramp fitting to derive the count rate (see Birkmann[11] and Böker et al.[12] for a more detailed description of our pipeline). In addition, the step of interpixel capacitance (IPC) correction can be optionally applied before linearity correction. IPC is the capacitance that arises between adjacent detector pixels in the source-follower CMOS design[13] and leads to coupling of signal between those pixels via displacement currents flowing from the collection node. In our preprocessing pipeline, this correction step is implemented by convolving each group image with an appropriate 3×3 kernel computed from the IPC coupling coefficient following McCullough.[14] The IPC coupling was derived by the NIRSpec DS team using a variety of methods (see next section). By default, we do not apply the step of IPC correction to NIRSpec data, so in the following description of the data analysis we will explicitly state when this step is applied.

Finally, our processing pipeline has the option of performing optimal up-the-ramp fitting using predefined weights as prescribed in the algorithm described by Fixsen et al.,[15] or simply using a linear least squares straight line fit to the

Table 1 Median value of the total noise (in e$^-$ rms) for the two H2RG SCAs in NIRSpec focal plane, for different levels of illumination, compared with prediction from Eq. (1).

	SCA491		SCA492	
	Data	Eq. (1)	Data	Eq. (1)
Darks ($i_{\text{dark}} \sim 7 \cdot 10^{-3}$ e$^-$ s^{-1})	7.2	5.5	6.5	5.2
Low flux ($f \sim 1.2$ e$^-$ s^{-1})	17.8	17.1	16.8	16.2
Low flux ($f \sim 1.2$ e$^-$ s^{-1}) – IPC corrected	18.4	17.1	17.5	16.1
High flux ($f \sim 150$ e$^-$ s^{-1})	269.1	315.1	262.8	307.4
High flux ($f \sim 150$ e$^-$ s^{-1}) – IPC corrected	278.0	314.9	273.8	307.4

data to determine the slope. Both methods are unbiased estimators and give the same mean slope value, but the equal-weight linear fit is nonoptimal in terms of signal-to-noise. For the purpose of this exercise, however, we opted for the linear least squares line fit, for which Eq. (1) applies.

Once processed, all count rate images for a given level of illumination were then combined to derive a map of the mean count rate and its standard deviation (in e$^-$ s^{-1}). The standard deviation map multiplied by the exposure effective integration time,[9] $t_{\text{int}} = (n-1)t_g$, provides a map of the total noise. In Table 1, the median values of the total noise distribution, computed across the entire detector array, for the darks and the two levels of incident flux are compared to the expected noise level. The latter are also the median values of the distribution (across the array) of the expected total noise, derived from Eq. (1), using the σ_{read} map and the mean count rate map (as f) for a given data set.

As shown in Table 1, the observed total noise in dark exposures is ~25% higher than predicted for an ideal detector with the same read noise (as derived from CDS noise). Moseley et al.[16] have carried out a principal component analysis of the read noise in similar detectors and found it to be dominated by a component with a $1/f$ spectrum. This component is not fully characterized by the CDS noise, therefore explaining the discrepancy between predicted and observed total noise in this case. Indeed, one can use Eq. (1) to estimate the value of an effective read noise, defined as the value of σ_{read} required for the computed total noise to match the observed value in darks. For a MULTI-88 × 1 exposure, this is ~18 e$^-$. The effective read noise to be used for Eq. (1) to match the measured value depends on the number of groups in the dark exposures; the longer the exposure the higher the effective σ_{read} value, as the effects of the $1/f$-read noise component accumulate.

At low flux levels, the measured median total noise values are in better agreement with the values computed from Eq. (1), using the same σ_{read} map as used for the darks and, as f, the mean count rate map for these exposures (cf. Table 1). The presence of IPC in these detectors, however, has the effect of spuriously lowering the observed noise level compared to the prediction of Eq. (1). Due to IPC, charge that is accumulated in one pixel is partly detected in the four neighboring pixels (at the level of ~1% per each 4-neighbor), thereby introducing a correlation among the signal of adjacent pixels. We investigated this effect by applying IPC correction when processing all the 50 "low-flux" exposures and generating from these new mean flux and total noise maps. As shown in Table 1, correcting for IPC leads to a 3% to 4% higher noise level and hence to a higher discrepancy between predicted and measured values. This discrepancy, however, can be explained in terms of the $1/f$-read noise component not accounted for by the CDS noise. Indeed, by substituting in Eq. (1) the effective read noise value for a MULTI-10 × 1 exposures (which is ~14 e$^-$), one finds that the computed median total noise value agrees well with that measured from the IPC-corrected exposures.

At high flux level ($f \sim 150$ e$^-$ s^{-1} pixel^{-1}) the comparison between computed and measured total noise is more surprising. As can be seen from Table 1, the measured total noise appears to be ~15% lower than that of an ideal system, as computed from Eq. (1). Correction for IPC reduces this discrepancy only marginally. At these flux levels, the total noise of the exposure is completely dominated by the Poissonian fluctuations in the photon field, expressed in Eq. (1) by the second term, since in our case $m = 1$ and the third term of Eq. (1) is zero. We note that even by taking the simple Poissonian noise of the total number of accumulated counts, one derives an (under-)estimate of the total noise of ~290 e$^-$, which is however still higher than the observed total noise.

We investigated whether the discrepancy between observed and predicted noise is dependent on the signal accumulated in the pixel potential well by looking at the difference between predicted noise levels and measured ones, as a function of the number of groups used to derive each exposure count rate. Note that, although these exposures were acquired with MULTI-88 × 1 pattern, at this flux level most pixels reach saturation by $n = 53$. When computing the expected noise level for each individual pixel, the number of groups used by the pipeline to derive the count rate in that pixel is being used in Eq. (1).

As shown in Fig. 1, indeed, the difference between the noise level theoretically expected and the one observed by computing the standard deviation of the count rate across the 25 high-flux exposures increases steadily with the number of groups, i.e., with the signal accumulated in the pixels ($N_{\text{e}^-} = n \cdot t_g \cdot f$), reaching the maximum level close to the pixel full well capacity.

4 Signal-Dependent Pixel-to-Pixel Correlations

An obvious interpretation for the noise "deficiency" observed at high counts could be the presence of extra interpixel correlation on top of the known IPC level.

For the purpose of characterizing the magnitude of interpixel crosstalk, and following Moore et al.,[13] charge appearing electrically in surrounding pixels can be described in terms of a single variable α, defined as the percent of total charge seen in any of the four nearest neighbor pixels. In other words, neglecting "second neighbor" and "diagonal neighbor" coupling and assuming two-dimensional symmetry in nearest neighboring pixels, the center node loses 4α of its charge, i.e., 1α to each of its four nearest neighbors. This can also be represented in terms of a 3×3 impulse-response array as

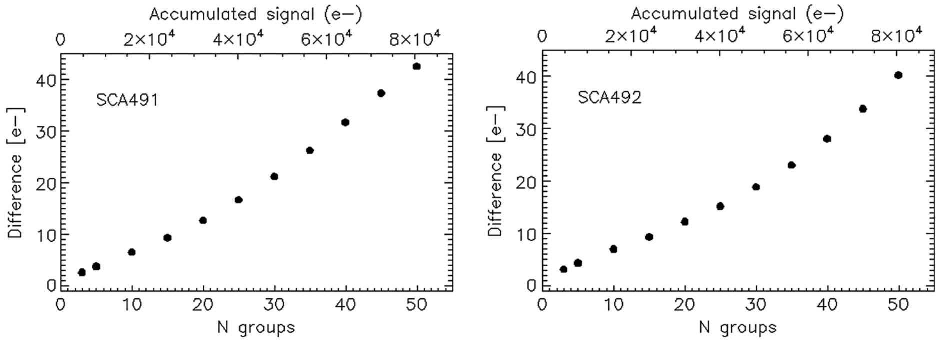

Fig. 1 Difference between the total noise level predicted using Eq. (1) and the observed value, as a function of the number of groups used to derive the count rate image in each of the 25 high-flux exposures, for the two NIRSpec detectors. At this flux level ($f \sim 150$ e$^-$ s^{-1}) most pixels reach saturation by group 53.

$$K\begin{pmatrix} 0 & \alpha & 0 \\ \alpha & 1-4\alpha & \alpha \\ 0 & \alpha & 0 \end{pmatrix}. \tag{2}$$

The IPC for these detectors was characterized by the NIRSpec DS team using a variety of methods: hot pixels, cosmic-ray events (CRE), and noise autocorrelation matrix (see Rauscher et al.[8] for a description of these three methods). For both SCAs of FPA 104, all three methods gave consistent results, with α~0.01. More specifically, with these methods, a 3×3 array representing the IPC-coupling to the central pixel for each SCA output can be derived; these arrays are those used by our pipeline to deconvolve each frame for the known IPC effect (as mentioned in Sec. 3). All three methods, however, sampled signal levels up to ~12,000 e$^-$ only, while, as shown in Fig. 1, the discrepancy that we observe between predicted and observed total noise starts to be significant when using exposures with at least 15 groups that, at a flux of ~150 e$^-$ s^{-1}, correspond to integrated signals of ~25,000 e$^-$.

To explore the hypothesis that the noise "deficiency" observed at high counts could be due to an increasing level of interpixel crosstalk somehow dependent on the pixel accumulated electrical signal, we extended the analysis of the pixel crosstalk using hot pixels with signals up to ~45,000 counts. From multiple dark exposures, we created a high signal-to-noise up the ramp cube, where isolated hot pixels with no hot or defective neighbor within five pixels were identified. Regions of 3×3 pixel size were extracted around each isolated hot pixel, background subtracted, and normalized by the value of the central hot pixel. All selected hot pixels were then grouped in bins of increasing accumulated signal, with each bin including between a few hundreds to a few thousands pixels. Median values of the 3×3 regions over all hot pixels within a given bin of accumulated signal were calculated and used to derive the value of α. The result of this analysis is shown in Fig. 2: the value of α appears to be overall constant across a large range of accumulated signal, similar to the results obtained by Hilbert and McCullough[17] and Cheng.[18]

Note, however, that in hot pixels the signal is not due to photon-generated charges but due to defects or impurities in the crystal lattice. Thus, to test the possibility that additional interpixel crosstalk could somehow depend on the level of photon-generated charge collected by a pixel, we computed the noise autocorrelation of different frames using 24 of the 25 high-flux exposures, coupled in 12 independent pairs. This was done according to the following procedure. (1) Each frame in every exposure is "reference pixel subtracted";[11] this correction uses the four rows of reference pixels at the top and bottom of each detector frame. For each of the four video outputs, and independently for odd/even columns, the mean value of the reference pixels is subtracted from each pixel value of the corresponding output. (2) For each exposure, a CDS difference between group n and group 1 is computed, and the difference of the two corresponding CDS images in an exposure pair provides a noise image with the signal removed: $\text{noise}_n = \text{CDS}_2(n) - \text{CDS}_1(n)$, where CDS_1 and CDS_2 indicate the CDS difference for exposures 1 and 2 of each pair of exposures. This noise image is then "destriped" (i.e., for each row in the detector, the average

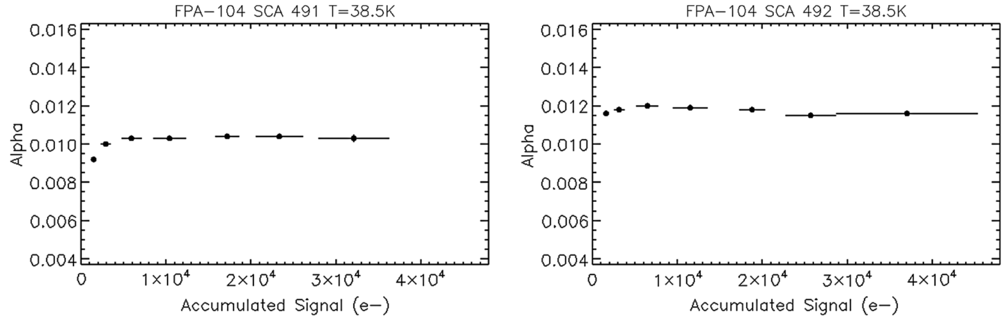

Fig. 2 The value of the pixel-to-pixel coupling coefficient α as derived from the analysis of 4-neighbors of hot pixels, as a function of the signal in the hot pixel—see text.

value for a row is subtracted from all the pixel values in that row) to reduce the correlation (in row direction) introduced by the $1/f$-noise component of the read noise. (3) The autocorrelation (c) is then computed over all operable pixels (x, y) of this noise image that have no inoperable pixels [an inoperable pixel is either a statistical outlier or a pixel having dark total noise $> 12\,e^-$ or differential quantum efficiency (DQE) < 70% of the average DQE] within a neighborhood of 3×3 pixels as

$$c_n(i,j) = [1/c_n(0{,}0)]\sum_{xy}\text{noise}_n[x,y]\cdot\text{noise}_n[x+i,y+j],$$
$$i,j \in [0{,}3]. \tag{3}$$

(4) The final autocorrelation matrix for group n is taken to be the median of all autocorrelation matrices computed from all independent pairs of observations (12 pair in total), for that group. This was computed for groups $n = (3{,}5{,}10{,}15,\ldots,40{,}45)$, for both SCAs; since a large fraction of pixels are saturated by $n = 45$ and about half are inoperable or neighbors to inoperable pixels, for $n > 45$ there are not enough valid pixels left to compute a meaningful autocorrelation.

As an example, the median correlation matrix for $n = 20$ is reproduced below.

$$c_{20} = \begin{pmatrix} 1.0000 & 0.03807 & 0.0019 & -0.0003 \\ 0.0365 & 0.00804 & 0.0009 & 0.0000 \\ 0.0023 & 0.00063 & 0.0010 & -0.0003 \\ 0.0004 & 0.00012 & 0.0007 & 0.0004 \end{pmatrix}. \tag{4}$$

The value of α (for small values of α) is approximated by

$$\begin{aligned} b &= [c(1{,}0) + c(0{,}1)]/2 \\ \alpha &= b/2 - b^2 \end{aligned}. \tag{5}$$

For low number of groups, however, the correlation matrices appear to be asymmetrical, with $c(1,0)$ systematically higher than $c(0,1)$, because of the additional correlation present in the row direction due to the $1/f$ noise which is not completely removed by the destriping step. Thus, to compute α we set $b = c(0{,}1)$.

The value of α derived in this way is plotted in Fig. 3 as a function of the number of electrons N_{e^-} accumulated at each group n for which the autocorrelation matrix was derived. From these graphs, one can see that α starts off at the known IPC value of ~0.01 at low counts and then increases as a function of the accumulated signal to reach a value of ~0.03 at $N_{e^-} \sim 75{,}000$ ($n = 45$), near pixel full well capacity. In the plots, the result of a least square fit with a quadratic polynomial is also shown; the fit coefficients for SCA491 and SCA492 are given in Table 2.

For accumulated signals N_{e^-} greater than ~10,000 e^-, these results clearly confirm the presence of an interpixel crosstalk component, which increases with the amount of photon-generated charge collected in the pixels, reaching, near the pixel saturation point, a coupling value α of about three times the IPC value as derived from hot pixels (in dark exposures). As described in the following sections, we have verified by simulations that this signal-dependent pixel-to-pixel crosstalk explains the discrepancy between predicted and observed total noise discussed in the previous section.

4.1 *Simulations*

To investigate whether the observed levels of pixel-to-pixel correlation could explain the noise deficiency observed in flat-field exposures we performed a Monte Carlo simulation of a flat-field exposure with SCA491, with flux intensity $f = 150\ e^-\ s^{-1}$. We simulated a data cube by incrementally adding integrated flux, one group at a time. The integrated flux during any given group time was distributed according to the Poisson distribution. Once all flux had been accumulated, each group was convolved with a kernel of the type given in Eq. (2), with the α value being determined by the average level of accumulated signal in that group, according to the relationship given by the polynomial fit for SCA491. Finally, normally distributed read noise ($\sigma_{\text{read}} = 12\,e^-$) was added to all pixels in all groups. To compute the total noise as a function of the number of groups, count rate images were derived from this simulated cube using different number of groups ($n = 3{,}5{,}10{,}15{,}20,\ldots$ etc.), and these were converted into integrated signal images

Table 2 Result of the fit to the values of α as a function of accumulated charge N_{e^-} with a polynomial $y = a_0 + a_1x + a_2x^2$ (as shown in Fig. 3).

	a_0	a_1	a_2
SCA491	8.9×10^{-3}	2.3×10^{-7}	9.0×10^{-13}
SCA492	1.1×10^{-2}	1.2×10^{-7}	1.7×10^{-12}

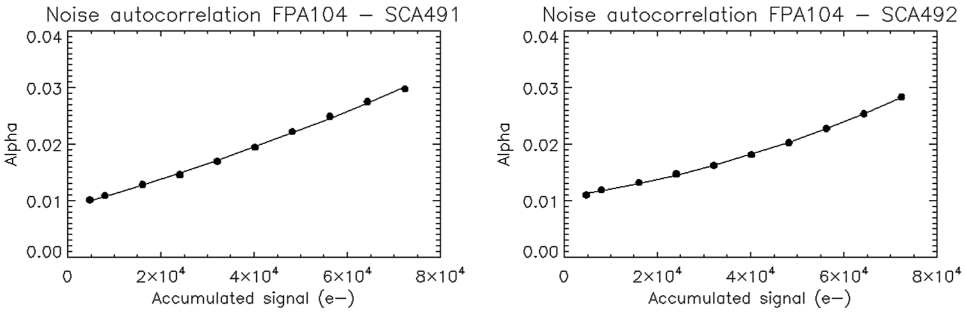

Fig. 3 The value of the pixel-to-pixel coupling coefficient α, as derived from the noise autocorrelation matrix as a function of the signal accumulated in the pixel potential well (dots). The fit to the data with a quadratic polynomial is given by the solid line.

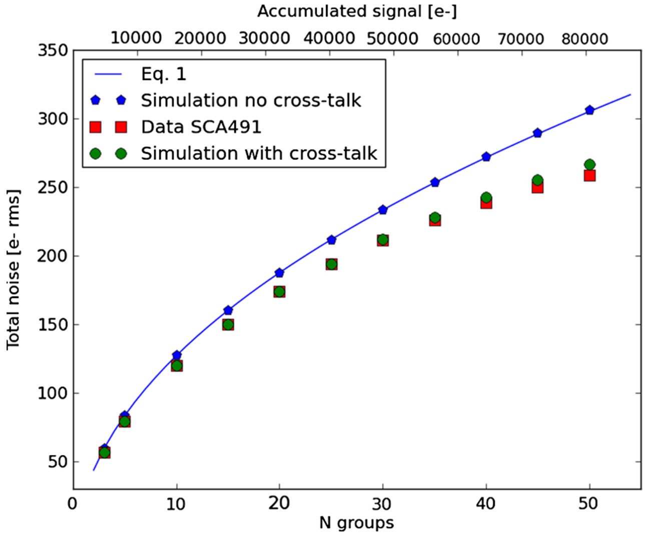

Fig. 4 Comparison between total noise levels as a function of the number of groups in simulated data (circles) and real data (squares). The level predicted by Eq. (1) is shown by the solid line. In the data, noise levels are lower than expected because of the effect of signal-dependent interpixel crosstalk. In the simulations this effect was reproduced by convolving each simulated group with a signal-dependent kernel of the type given in Eq. (2) (see text).

by multiplying by the integration time; the standard deviation of each one was then calculated. The results are shown in Fig. 4, together with the prediction from Eq. (1) (in the absence of interpixel crosstalk) and the total noise from SCA491 for high-flux flat-field illumination, derived for different number of groups, as described in Sec. 3. For completeness, the results of the simulation in the absence of the convolution step, i.e., the ideal case, is also shown.

From Fig. 4, one can see that once the effect of the observed signal-dependent interpixel crosstalk is included, the total noise of the simulated data reproduces well the total noise measured in the real data. This confirms that the pixel-to-pixel signal-dependent correlation observed in the data noise maps is at the origin of the observed noise discrepancy.

In the simulations, however, total noise levels are slightly higher [and therefore less discrepant from Eq. (1)], for higher number of groups than in the real data. This is not surprising given the simplifying assumptions on interpixel coupling as represented by the kernel used in the simulations [Eq. (2)], which neglects "diagonal neighbor" and "second neighbor." If coupling to "diagonal neighbor" and "second neighbor" were truly negligible, then the values of $c(1,1)$ and $c(2,0)$ or $c(0,2)$ in the correlation matrix would be, respectively, $2\alpha^2$ and α^2. However, we see that, in all autocorrelation matrices computed in the previous section [see for example Eq. (4)], coefficients $c(1,1)$ and $c(2,0)$ are significantly higher than $2\alpha^2$ and α^2 and indeed their value increases, relatively to α, with the level of accumulated signal. Since this additional interpixel coupling to more distant neighbors is not modeled in the simulation, the derived total noise is expected to be slightly higher than in the real data.

5 Discussion and Conclusions

In these detectors, crosstalk between pixels can be caused by two independent phenomena, IPC and charge diffusion. IPC is caused by capacitive coupling between adjacent pixels[13] while charge diffusion is the lateral movement (pixel-to-pixel) of charge between the points of charge production and charge collection in the bulk of the detector. While charge diffusion is a stochastic process that obeys Poissonian statistics, IPC is a deterministic process that leads to noise correlation and hence to pixels displaying "sub-Poissonian" noise.[13,19] As described in the previous sections, for high levels of accumulated signal, our detectors have sub-Poissonian noise levels and display signal-dependent noise correlations. Therefore, to explain our data, we have to consider a deterministic crosstalk component, like IPC. Note that this does not rule out the presence of charge-diffusion in these detectors, although Finger et al.[20] have shown capacitive coupling between neighboring pixels to be the dominant contribution to the point spread function (PSF) of 2.5 μm-cutoff H2RG detectors.

Hilbert and McCullough[17] used hot pixels to study the IPC coupling between adjacent pixels probing signal up to 20,000 analog-to-digital units (ADUs) and see no significant variation in the coupling value with signal level. Cheng[18] studied the dependency with temperature, accumulated charge, and background level of the IPC effect in HgCdTe detectors. From Figs. 5.7 and 5.8 in that work, IPC coupling measured from hot pixels and CRE in dark exposures appear to initially decrease with accumulated counts from ∼0.02 to ∼0.01 at 5000 ADUs but then to stay roughly constant up to 30,000 ADUs. Conversely, when looking at CRE in illuminated exposures (flat illuminations), Cheng[18] finds that the IPC coupling appears to increase from 0.01 to ∼0.03 (see Fig. 5.12 of his thesis), for background levels from 0 to 16,000 ADUs. These findings, if confirmed, appear to suggest that IPC coupling between the central pixel and its neighbors is influenced by the background levels.

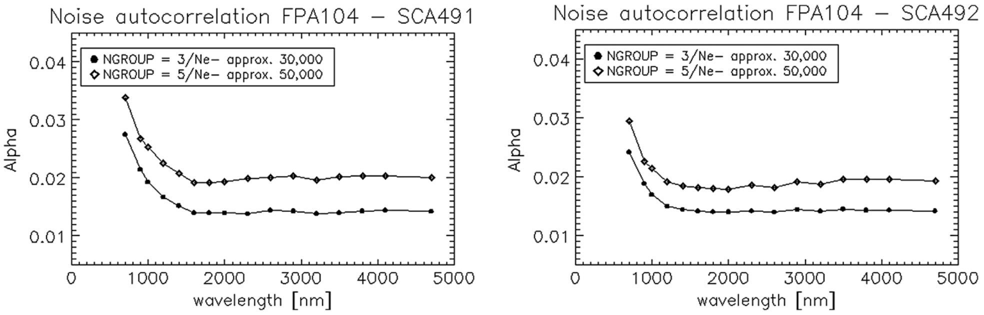

Fig. 5 The dependency of α with wavelength as derived from the noise autocorrelation matrix of monochromatic flat fields. The quantum yield exceeds unity for λ lower than ∼1.4 μm.

Apart from the initial drop in coupling value when using hot pixels (that we do not see in our data), our findings are in agreement with those of Cheng.[18] We also see α being overall constant with the accumulated signal when looking at the coupling between hot pixels and their neighbors in dark exposures, while α clearly increases with accumulated charge, when looking at the noise correlation in intensely illuminated exposures.

An increase of interpixel coupling with accumulated signal or background level cannot be easily explained in terms of the current IPC model. In the model of IPC developed by Moore et al.,[13,19] the detector array of photodiodes is represented as an array of capacitors, each with identical capacitance C_0, and the IPC is represented by small coupling capacitors between the nodes, C_c. The interpixel coupling α depends on the ratio C_c/C_0.[21] In these detectors the node capacitance increases as a function of voltage (i.e., as a function of accumulated charge), so that α would be expected to decrease with accumulated charge. While it is not easy to model the cross-coupling parasitic capacitance between the pixels, the current model predicts also C_c to decrease as the nodes collect photocarriers.[19] This means that α would be expected to decrease with signal, but we observed the opposite.

From a phenomenological point of view, if this signal-dependent interpixel crosstalk is linked to the IPC effect, one would expect its intensity to be independent of the wavelength of the incident photons. Following the noise autocorrelation approach described in Sec. 4, we have derived the value of α as a function of wavelength using the monochromatic flat fields acquired during the DS tests for quantum efficiency characterization. In this case, the flux is very strong, with $f \sim 930\ \mathrm{e^-\,s^{-1}}$ at 2.6 μm, so that only five groups were acquired per exposure. Figure 5 shows the value of α as a function of wavelength, as derived from the noise correlation matrix computed for groups 3 and 5 in these exposures (only one exposure pair at each wavelength was used in this case). Also in this case the value of α increases with accumulated charge, i.e., with the number of groups. Below 1.6 μm, α increases steeply with wavelength, but at these wavelengths the detector quantum yield becomes greater than one, i.e., more than one electron is being produced by each photon detected by the sensor. As shown by McCullough et al.[22] and Fox et al.,[23] in this type of detectors the quantum yield exceeds unity for $\lambda < 0.28\lambda_{\mathrm{co}}$, where λ_{co} is the cut-off wavelength, so for $\lambda < 1.5\ \mu$m our noise model does not apply and we cannot easily quantify the dependency of the signal-dependent crosstalk term with wavelength. From 1.6 to 5 μm, however, the value of α appears to be essentially independent of wavelength, consistent with this interpixel crosstalk term being generated by an IPC-type effect. Note that the high-flux flat-field exposures described in Sec. 3 were obtained using a black-body source peaked at $\sim$5 μm, so those exposures are minimally affected by quantum yield larger than 1. In Fig. 5, the values of α for $\lambda > 1.6\ \mu$m can be compared to those derived in the previous section (and are indeed very similar for the corresponding levels of accumulated charge).

In summary, we have reported here the presence, in the two NIRSpec H2RG detector arrays, of an interpixel crosstalk component that increases with accumulated charge. This effect is significant, reaching a coupling of 3% near pixel full well. The data presented here only probe the difference in crosstalk behavior between hot pixels in dark exposures and normal pixels in flat-field exposures, and this does not allow us to establish whether the observed increase in crosstalk depends on the signal accumulated by any normal pixel individually or on similar level of signal being mutually accumulated in adjacent pixels.

In the first case, a 3% coupling near pixel full well capacity would imply that, for $N_{\mathrm{e^-}} > 50{,}000$, a significant fraction of the signal from a strongly illuminated pixel could appear in faintly illuminated adjacent pixels. This would result in a signal-dependent widening of the PSF, thus impacting the instrument scientific performance. Indeed, from a preliminary analysis of NIRSpec data acquired during the first cycle of the calibration and performance verification campaign, we see evidence of wider than expected wings (and anomalous integration ramps) at the edge of bright spectra, which can be explained by signal-dependent interpixel crosstalk.[24]

Although the evidence from this study is that the crosstalk is of deterministic nature like the IPC effect (and unlike charge diffusion), the current IPC model cannot explain its dependency with signal. To improve the characterization of this crosstalk term, we plan to acquire specific data during the second cycle of NIRSpec calibration and performance verification campaign[25] and will describe the impact of this effect on the instrument performance in a future work.

Acknowledgments

We thank Samuel Harvey Moseley and Markus Loose for very useful discussions.

References

1. J. P. Gardner et al., "The James Webb Space Telescope," in *Astrophysics in the Next Decade, Astrophysics and Space Science Proceedings*, H. A. Thronson, M. Stiavelli, and A. Tielens, Eds., p. 978, Springer, Netherlands (2009).
2. J. W. Beletic et al., "Teledyne imaging sensors: infrared imaging technologies for astronomy and civil space," *Proc. SPIE* **7021**, 70210H (2008).
3. R. J. Laureijs et al., "The Euclid mission," *Proc. SPIE* **7731**, 77311H (2010).
4. M. Robberto et al., "Selection of the infrared detectors for Wide Field Camera 3 on the Hubble Space Telescope," *Proc. SPIE* **5167**, 166–174 (2004).
5. P. J. McGregor et al., "Near-infrared integral-field spectrograph (NIFS): an instrument proposed for Gemini," *Publ. Astron. Soc. Aust.* **16**(3), 273–287 (1999).
6. S. D'Odorico et al., "X-shooter: UV-to-IR intermediate-resolution high-efficiency spectrograph for the ESO VLT," *Proc. SPIE* **5492**, 220–229 (2004).
7. M. Loose et al., "High-performance focal plane arrays based on the HAWAII-2RG/4G and the SIDECAR ASIC," *Proc. SPIE* **6690**, 66900C (2007).
8. B. J. Rauscher et al., "James Webb Space Telescope near-infrared spectrograph: dark performance of the first flight candidate detector arrays," *Proc. SPIE* **7021**, 702124 (2008).
9. B. J. Rauscher et al., "Detectors for the James Webb Space Telescope near-infrared spectrograph. I. Readout mode, noise model, and calibration considerations," *Publ. Astron. Soc. Pac.* **119**(857), 768–786 (2007).
10. B. J. Rauscher et al., "Erratum," *Publ. Astron. Soc. Pac.* **122**(896), 1254 (Erratum) (2010).
11. S. Birkmann, "Description of the NIRSpec pre-processing pipeline," NIRSpec Technical Note NTN-2011-004, ESA/ESTEC, (2011), http://www.rssd.esa.int/doc_fetch.php?id=3100534.
12. T. Böker et al., "The spectro-photometric calibration of the JWST NIRSpec instrument," *Proc. SPIE* **8442**, 84423F (2012).
13. A. C. Moore, Z. Ninkov, and W. J. Forrest, "Interpixel capacitance in nondestructive focal plane arrays," *Proc. SPIE* **5167**, 204–215 (2004).

14. P. McCullough, "Interpixel capacitance: prospects for deconvolution," Instrument Science Report WFC3 2008-26, Space Telescope Science Institute (2008).
15. D. J. Fixsen et al., "Cosmic-ray rejection and readout efficiency for large-area arrays," *Publ. Astron. Soc. Pac.* **112**(776), 1350–1359 (2000).
16. S. H. Moseley et al., "Reducing the read noise of H2RG detector arrays: eliminating correlated noise with efficient use of reference signals," *Proc. SPIE* **7742**, 77421B (2010).
17. B. Hilbert and P. McCullough, "Interpixel capacitance in the IR channel: measurements made on orbit," Instrument Science Report WFC3 2011-10, Space Telescope Science Institute (2011).
18. L. Cheng, "Interpixel capacitive coupling," MS Thesis, Center for Imaging Science—Rochester Institute of Technology (2009).
19. A. C. Moore, Z. Ninkov, and W. J. Forrest, "Quantum efficiency overestimation and deterministic crosstalk resulting from inter-pixel capacitance," *Opt. Eng.* **45**(7), 076402 (2006).
20. G. Finger et al., "Interpixel capacitance in large format CMOS hybrid arrays," *Proc. SPIE* **6276**, 62760F (2006).
21. G. Finger et al., "Conversion gain and interpixel capacitance of CMOS hybrid focal plane arrays," in *Scientific Detectors for Astronomy 2005*, J. E. Beletic, J. W. Beletic, and P. Amico, Eds., p. 477, Springer, Netherlands (2006).
22. P. R. McCullough et al., "Quantum efficiency and quantum yield of an HgCdTe infrared sensor array," *Publ. Astron. Soc. Pac.* **120**(869), 759–776 (2008).
23. O. Fox et al., "The Fe 55 x-ray energy response of mercury cadmium telluride near-infrared detector arrays," *Publ. Astron. Soc. Pac.* **121**(881), 743–754 (2009).
24. G. Giardino et al., "NIRSpec detectors: noise properties and the effect of signal dependent inter-pixel crosstalk," *Proc. SPIE* **8453**, 84531T (2012).
25. S. M. Birkmann et al., "The near infrared spectrograph (NIRSpec) on-ground calibration campaign," *Proc. SPIE* **8442**, 84423E (2012).

Giovanna Giardino gained a PhD in astronomy from the University of Milano and then joined the European Space Agency in 1999 as a research fellow working on modeling of the galactic diffuse emission in preparation for the analysis of *Planck* data. She remained at the ESTEC center working on various scientific aspects of the *Planck* mission and data simulations while independently carrying out astronomical research in the field of star formation using mainly x-ray data. Three years ago, she joined the NIRSpec Scientific Operation Team and has been contributing to the instrument tests and calibration campaigns, focusing in particular on the characterization of NIRSpec detectors.

Biographies and photographs of the other authors are not available.